Electronic Supplementary Material (ESI) for Chemical Communications.

Supporting information

Three-Dimensional Bi_2O_3/Ti Microspheres as an Advanced Negative Electrode for Hybrid Supercapacitors

Experimental section

Materials:

All the chemicals used in this work were of analytical grade and used without further purification. Bismuth nitrate pentahydrate ($Bi(NO_3)_3.5H_2O$), cobalt nitrate hexahydrate ($Co(NO_3)_2.6H_2O$) from Sigma-Aldrich, ethylene glycol (EG), nickel nitrate pentahydrate ($Ni(NO_3)_2.6H_2O$), ammonium fluoride (NH_4F), acetone, isopropyl alcohol (IPA) and potassium hydroxide (KOH) from Hi-media, Hexamethylenetetramine from TCI chemical and commercially available titanium and nickel sheets were purchased.

Synthesis of 3D-Bi_2O_3/Ti flower-like microspheres as a negative electrode:

The binder-free 3D-Bi_2O_3/Ti nanostructure electrodes were synthesized by a two-step synthesis method i.e. solvothermal followed by annealing treatment. In this synthesis, 25 cm^3 of acetone and 6 cm^3 ethylene glycol with 0.3 g of $Bi(NO_3)_3.5H_2O$ were dissolved evenly by using a magnetic stirrer to obtain a transparent solution. The resulting transparent solution was transferred to a Teflon liner containing a cleaned Ti sheet. The Teflon liner was sealed inside a stainless steel autoclave, then kept inside a hot air oven and treated with 150 $^{\circ}$C for various times (10 min, 1, 3 and 6 h). After the autoclave gets cooled down naturally to room temperature, the as-prepared Bi_2O_3/Ti electrodes were taken out and cleaned with DI water followed by IPA and dried in an electric oven. The as-prepared electrodes were annealed at 250°C for 2 h (2 °C/m) under air to obtain binder-free 3D-Bi_2O_3/Ti electrodes.

Preparation of 3D-$NiCo_2O_4$/Ni nanostructures as a positive electrode:

The binder-free 3D-$NiCo_2O_4$/Ni nanostructure electrodes were also synthesized by a two-step synthesis method i.e. hydrothermal followed by thermal annealing treatment. In this preparation process 0.145 g and 0.291 g of (ratio 1:2) metal (Ni^{2+} : Co^{2+}) nitrates, 0.111 g of ammonium fluoride and 0.5606 g of hexamethylenetetramine were dissolved in 40 ml of DI water. The obtained pink colour solution was transferred to stainless steel Teflon liner

containing Ni sheet. The stainless steel container was kept inside an electric oven and treated with 100 ˚C for 6 h. After completion of the hydrothermal reaction, the sample was taken out and washed with DI water followed by acetone and dried in hot air oven. The as-prepared electrodes were annealed at 350 °C for 3 h (5 °C/min) under air to obtain binder-free 3D-$NiCo_2O_4$/Ni electrodes.

Structural characterizations:

The structural, morphological and elemental properties of the samples were examined through the X-ray diffraction (XRD, PANalytical, Netherlands), Fourier transform Infra-red spectroscopy (FTIR, SHIMADZU, IRTRACER 100), Scanning electron microscopy (SEM, ZEISS EVA-15), Field emission-scanning electron microscopy (FE-SEM, Tescan-Mira 3 LMH), Transmission electron microscopy (TEM, Jeol, TEM1400, Japan) and Energy dispersive X-ray spectroscopy analysis (EDS, Bruker Quantax 200). Further, the chemical composition of the as-prepared sample was evaluated by X-ray Photoelectron spectroscopy (XPS, Omicron ESCA (Electron Spectroscope for Chemical Analysis)). The surface area and porosity were evaluated through N_2 adsorption-desorption isotherms (BET, Micromeritics, ASAP-2020, USA) measurements.

Electrochemical measurements:

All the electrochemical experiments were carried out using PARSTAT MC-1000 Electrochemical Workstation using the software VERSA STUDIO. The individual working electrode were performed with a three-electrode system, and a mercury/mercury oxide as reference electrode (Hg/HgO in 1 M NaOH) and a platinum as counter electrodes were used along with 1.0 M KOH aqueous electrolyte. The electrochemical parameter such as areal capacitance (F cm^{-2}) of the as-prepared electrode was calculated from the cyclic voltammetry, and Galvanostatic charge-discharge curves by using equations (1) and (2) respectively [1].

$$C_A = \frac{\int I.dV}{2\Delta V.A.S} \quad (1)$$

$$C_A = \frac{I.\Delta t}{A.\Delta V} \quad (2)$$

where, I (A) is the response current (CV), ΔV (V) is the voltage window, S (V/s) is the scan rate, A (cm^2) is the active area of the electrode, I (A) is the constant current density of GCD (cm^2), Δt (s) is the discharging time.

Fabrication of 3D-$NiCo_2O_4$‖Bi_2O_3 hybrid supercapacitors:

A 3D-$NiCo_2O_4$‖Bi_2O_3 hybrid supercapacitors was assembled in standard electrochemical test cell using 3D-$NiCo_2O_4$/Ni as positive electrode and Bi_2O_3/Ti as negative electrode with filter paper as the separator in the middle. Herein, a few drops of 1 M KOH aqueous solution served as the electrolyte. A two-electrode cell system was applied to examine the device performance of the added 3D electrodes. The areal capacitance, energy and power densities of the hybrid device were calculated based on the total electroactive area of both the positive (1 cm^2) and negative (1 cm^2) electrodes using the following equations (3) and (4)[1];

$$E = 0.5\frac{CV^2}{3.6} \quad (3)$$

$$P = 3600\frac{E}{\Delta t} \quad (4)$$

Herein, E is energy density (Wh cm^{-2}), P is power density (W cm^{-2}), C is the areal capacitance of the device (F cm^{-2}), ΔV (V) is the voltage window, Δt (s) is the discharging time.

Results and discussion:

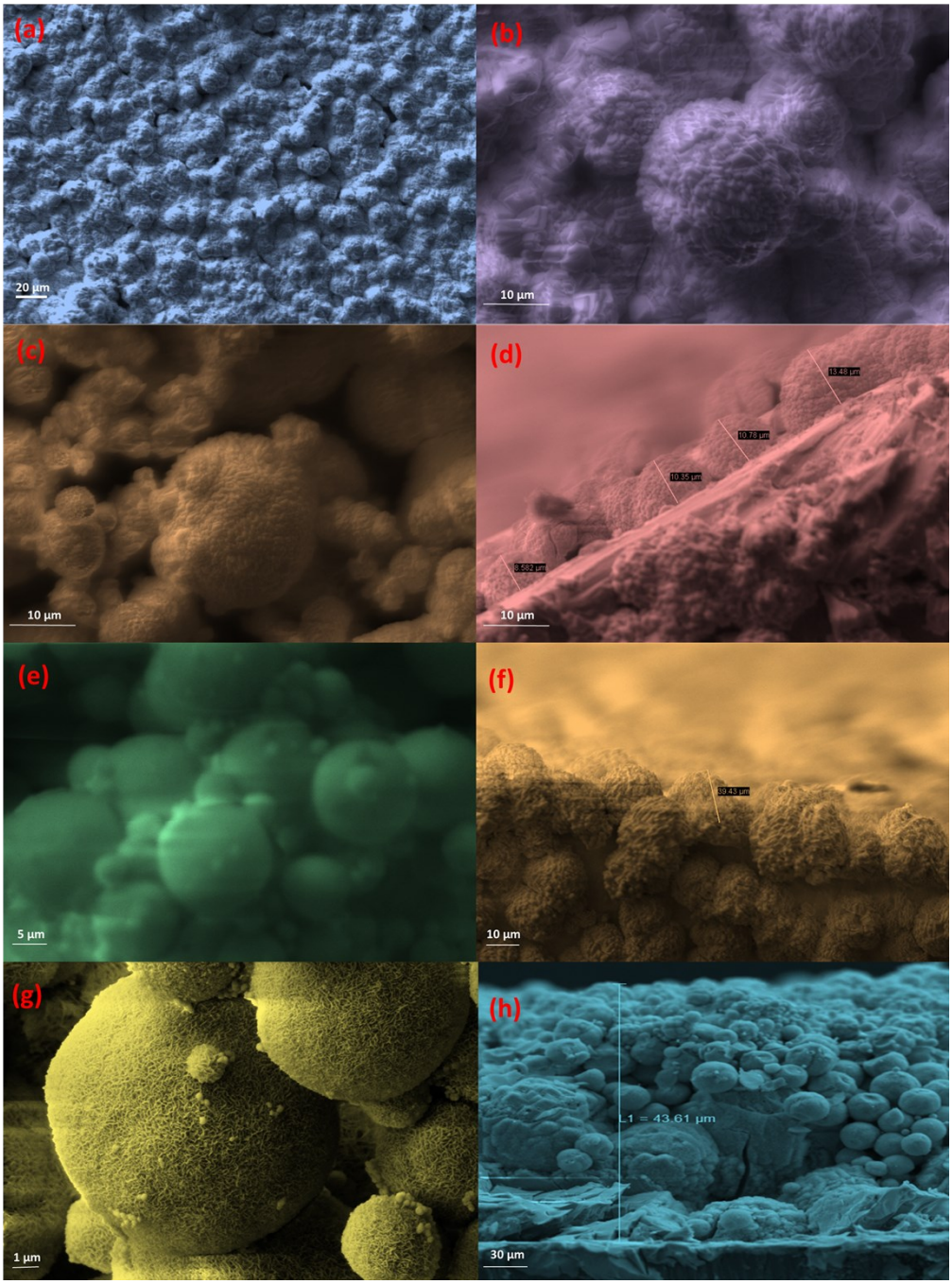

Fig. S1 Growth mechanism of 3D-Bi_2O_3 microsphere with respect to different reaction time (a and b: 10 min, c and d: 1 hour, e and f: 3 hour, g and h: 6 hour).

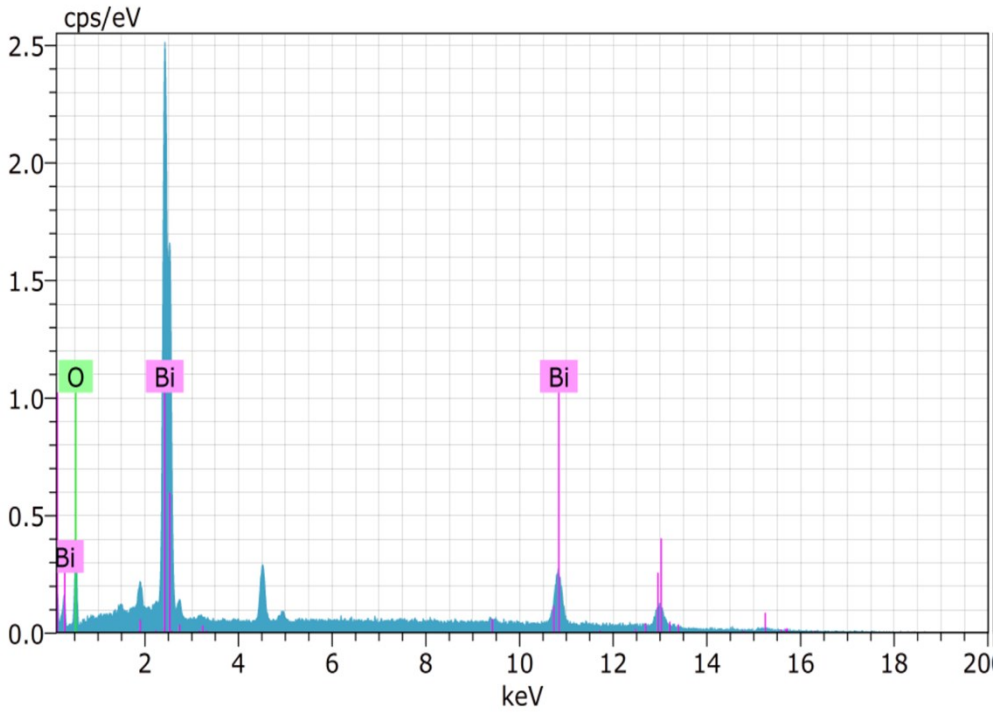

Fig. S2 EDX spectrum of 3D-Bi_2O_3/Ti electrode.

Fig. S2 shows the EDX mapping indicates the presence of Bi and O element in the flower-like Bi_2O_3 microsphere structure.

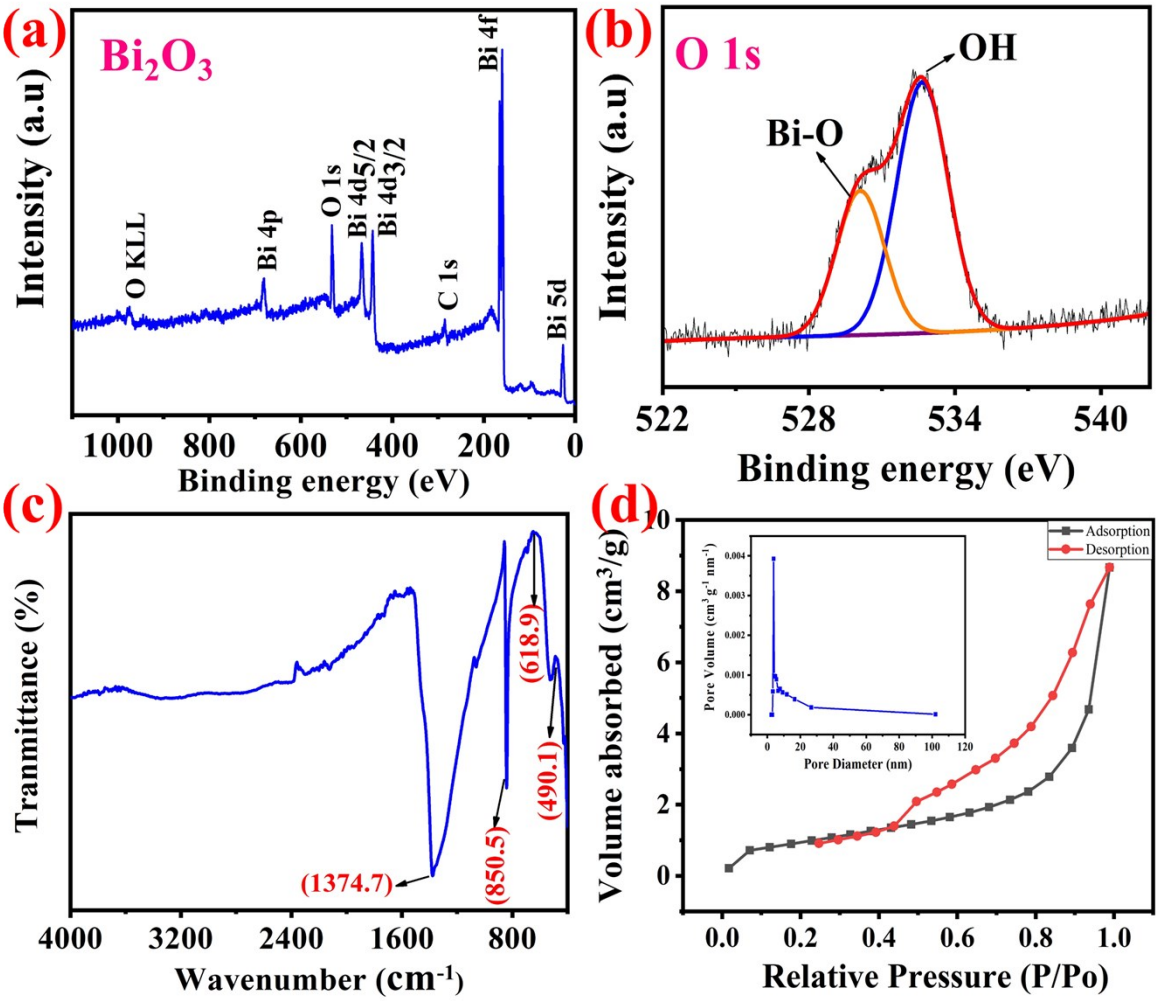

Fig. S3 (a) XPS survey spectrum of 3D-Bi_2O_3/Ti electrode, (b) High- resolution XPS-spectrum of O1s (c) FTIR spectrum of 3D-Bi_2O_3/Ti electrode and (d) BET analysis of 3D-Bi_2O_3/Ti electrode.

The functional groups present in the as synthesised 3D Bi_2O_3/Ti electrode was analysed through Fourier transform infrared spectroscopy (FTIR). The peaks appeared at 490 and 619 cm^{-1} corresponds to the bending vibration of Bi-O bond and stretching vibration of O-Bi-O bond, respectively [2]. The other two peaks indicate the existence of interlayer nitrates in the Bi_2O_3 structure [3] and the results are shown in Fig S3c

The porous characteristics of flower-like 3D-Bi_2O_3 microspheres are examined by the N_2-adsorption/desorption isotherms. The presence of H_3-type hysteresis in midway of ca. 0.45/1.0 P/P_0 confirms the porous-type character of 3D-Bi_2O_3 microspheres with mesoporous as shown in Fig. S3d. The pore size distribution were calculated by desorption isotherm using Barret-Joyner-Halenda (BJH) method. The average pore diameter, surface area and average pore volume of 3D-Bi_2O_3 microspheres are about 3.759 nm, 6.7 m^2 g^{-1} and 0.015 cc g^{-1} respectively.

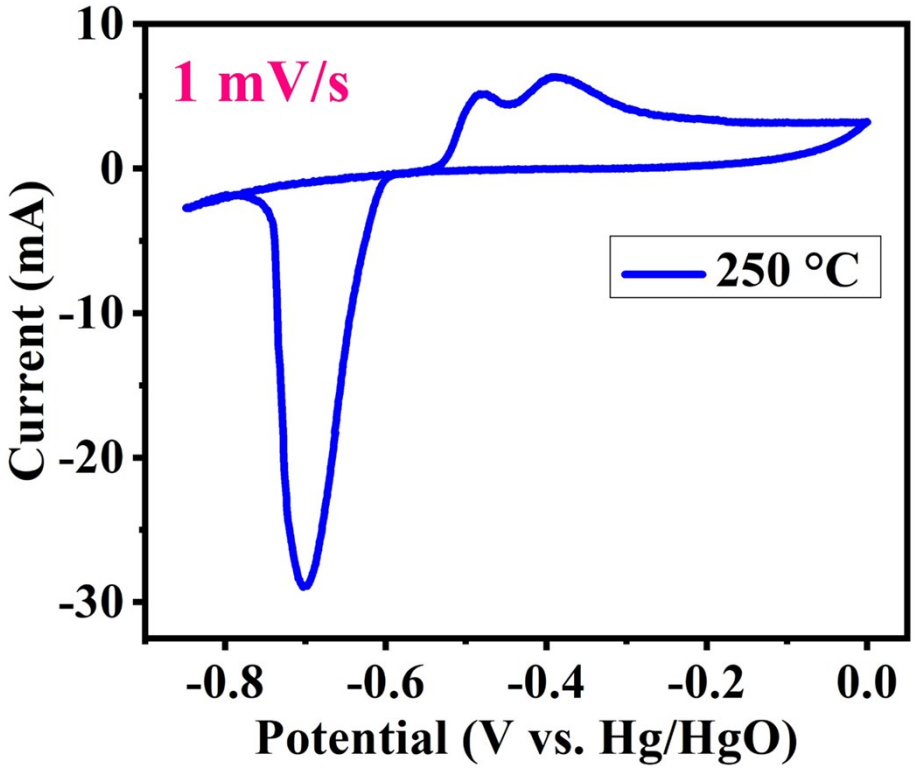

Fig. S4 CV curve at a scan rate of 1 mV s^{-1} of Bi_2O_3 electrode.

The charge storage mechanism of the Bi_2O_3 electrode material is expressed by simple chemical equation [4], such as,

$$Bi_2O_3 + H_2O + 2e^- \leftrightarrow Bi_2O_2 + 2OH^- \quad \text{.....(5)}$$

$$Bi_2O_2 + 2H_2O + 4e^- \leftrightarrow 2Bi + 4OH^- \quad \text{.....(6)}$$

Overall reaction:

$$Bi_2O_3 + 3H_2O + 6e^- \leftrightarrow 2Bi + 6OH^- \text{ .....(7)}$$

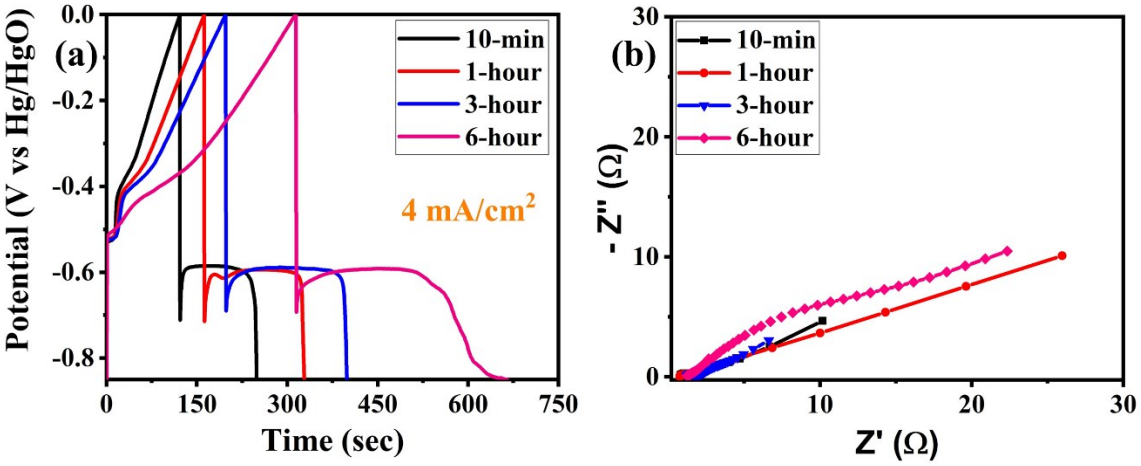

Fig. S5 (a) GCD and (b) Nyquist plots of Bi_2O_3 microspheres on Ti substrate at different growth times (10-min, 1-hour, 3-hour and 6-hour).

All of the GCD profiles (Fig. S5a) displayed the asymmetric discharges curves with potential plateau indicating the pseudocapacitive nature of the as-prepared electrodes. Further, the calculated areal capacitance is 0.60, 0.77, 0.93 and 1.65 F cm^{-2} for the 10 min, 1h, 3h and 6h deposited Bi_2O_3/Ti electrodes, respectively. With increasing the deposition time, as expected areal capacitance is increased, which indicated the highest performance of 6 h deposited 3D-Bi_2O_3/Ti electrode. This might be due to the higher mass loading of electroactive materials as well as optimum three-dimensional porous nanostructures. Further, the electrochemical impedance spectroscopy measurement (Fig. S5b) was performed to analyse the electronic and ionic conductivity of various thickness 3D-Bi_2O_3/Ti nanostructure electrode in the frequency range of 0.1 Hz to 1 M Hz. It is observed that the various thickness of 3D-Bi_2O_3/Ti nanostructure electrode exhibited the lesser solution and charge-transfer resistance indicating the better electrical conductivity of the as-prepared electrodes.

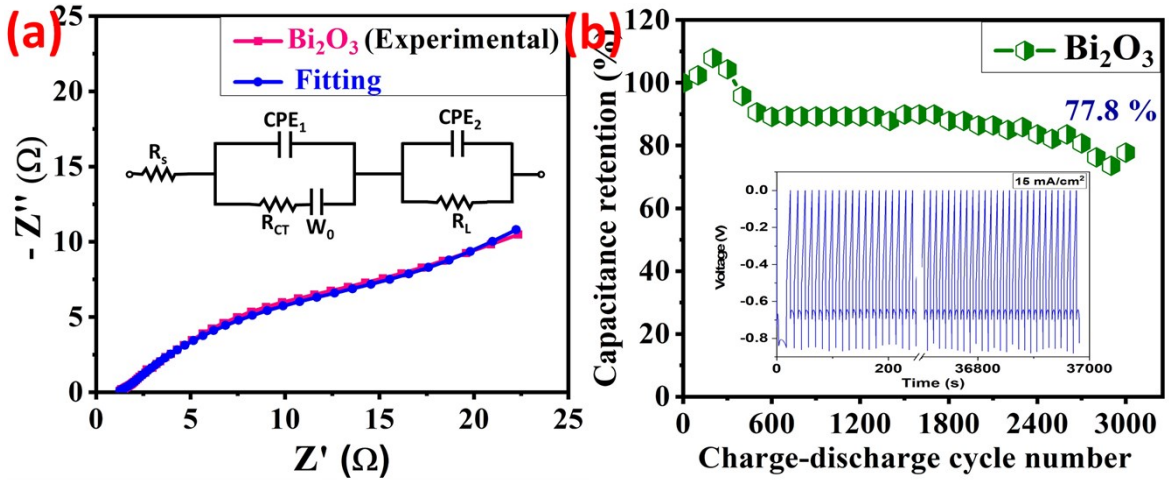

Fig. S6 (a) Nyquist plot of 3D-Bi_2O_3/Ti electrode, inset is the equivalent circuit and Bode plot of 3D-Bi_2O_3/Ti electrode, (b) Cycle stability test of the 3D-Bi_2O_3/Ti electrode. The inset shows a few initial and final cycles, which confirms the satisfactory stability of the electrode.

The Nyquist plot of the Bi_2O_3/Ti electrode is shown in (Fig. S6a, ESI†). The Bi_2O_3/Ti electrode exhibits a semi-circle at higher frequency region followed by a narrow line at low frequency region. Further, the Nyquist plots were fitted well with the equivalent circuit model and its fitted plots are presented in inset Fig. S6a, ESI†. Equivalent series resistance (ESR) is related to the resistance of the electrolyte (R_S), resistance of the current collector, and contact resistance at the active material/substrate interface. The diameter of the semicircle in the high frequency regions corresponds to the charge transfer resistance at the electrode/electrolyte interface caused by Faradaic redox process[5]. Further, the low charge transfer resistance of the electrode demonstrates the fast ion transport. Then the model consists of two constant phase elements (CPE_1 and CPE_2), followed by a Warburg impedance at the low frequency region indicating diffusion of electrolyte ions into the electrode materials. The CPE_2 at low frequency region might contain both double layer capacitance and faradaic capacitance which occurs at interfaces between electrode and electrolyte due to the separation of ionic and/or electronic charges[6]. Finally, R_L is the leakage resistance, which is parallel with constant phase element and it signifies faradaic capacitance. The fitted data of the circuit element is R_s= 1.082 Ω, R_{ct}

=18.2 Ω, CPE_{DL}= 0.01493 (Q_{DL}) and 0.6286 (n_{DL}), W_o= 0.09384, and CPE_L= 0.03919 (Q_L) and 0.4003 (nL).

Table. 1 Comparison of electrochemical parameters of supercapacitor negative electrode materials.

Sl. No.	Electrode material	Potential window	Electrolyte	Areal capacitance	Ref.
1.	CNT@600Fe_2O_3	-1.2 to 0 V	2 M KOH	659.5 mF cm^{-2} (5 mA cm^{-2})	7
2.	Porous graphene film electrode	-1.2 to 0 V	1 M KOH	249.1 mF cm^{-2} (2 mA cm^{-2})	8
3.	Fe_3O_4 nanotube	-0.8 to 0 V	5 M LiCl	180.4 mF cm^{-2} (1 mA cm^{-2})	9
4.	WO_3 nanowires	-1 to 0 V	1 M $LiSO_4$	800 mF cm^{-2} (1 mA cm^{-2})	10
5.	CF-WO_3@PPy	-1 to 0 V	3 M NaOH	253 mF cm^{-2} (0.67 mA cm^{-2})	11
6.	MoO_2/CC	-1 to 0 V	1 M Na_2SO_4	174.97 mF cm^{-2} (1.43 mA cm^{-2})	12
7.	Porous Mn_3O_4/NGP electrode	-0.8 to 0 V	1 M NaOH	372.5 mF cm^{-2} (1 mA cm^{-2})	13
8.	Microbelt-like 2D Bi_2O_3	-1 to 0 V	6 M KOH	309 mF cm^{-2} (2 A g^{-1})	14
9.	Bi_2O_3 nanoflower /CNF electrode	-0.9 to 0 V	1 M Na_2SO_4	545 mF cm^{-2} (3 mA cm^{-2})	15
10.	α-MoO_3 nanobelts	-1 to 0 V	1 M H_2SO_4	64 μF cm^{-2} (20 mV s^{-1})	16
11.	MoO_2 nanowire	-1 to 0 V	3 M LiCl	424.4 mF cm^{-2} (4 mA cm^{-2})	17
12.	Nanoflower-like WO_3	-0.5 to 0 V	1 M H_2SO_4	684.5 mF cm^{-2} (6 mA cm^{-2})	18
13.	3D-Bi_2O_3/Ti	-0.85 to 0 V	1 M KOH	1650.0 mF cm^{-2} (4 mA cm^{-2})	This work

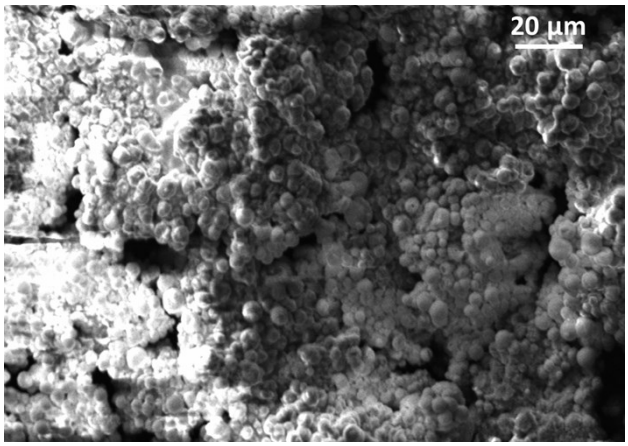

Fig. S7 FE-SEM image of 3D-Bi_2O_3/Ti electrode after 3000 charge-discharge cycles.

Positive electrode: 3D-$NiCo_2O_4$ nanostructure

3D-$NiCo_2O_4$/Ni nanostructure was directly grown on Ni current collector by hydrothermal method followed by the annealing process. The crystal structure and phase purity of $NiCo_2O_4$ was confirmed through XRD analysis as shown in Fig. S8 a. The peaks observed at 2θ=31.02°, 36.6°, 38.18°, 44.22°, 58.96°, 64.66° and 76.75° corresponds to (200), (311), (222), (400), (511), (440) and (622) planes of cubic $NiCo_2O_4$ matched well with standard JCPDS file no (20-0781). Fig. S8 (b – e) shows the SEM images of 3D-$NiCo_2O_4$-Ni electrode and it displays the well-defined 3D microsphere nanostructure is formed. The thickness of the 3D-$NiCo_2O_4$/Ni is ~85 µm.

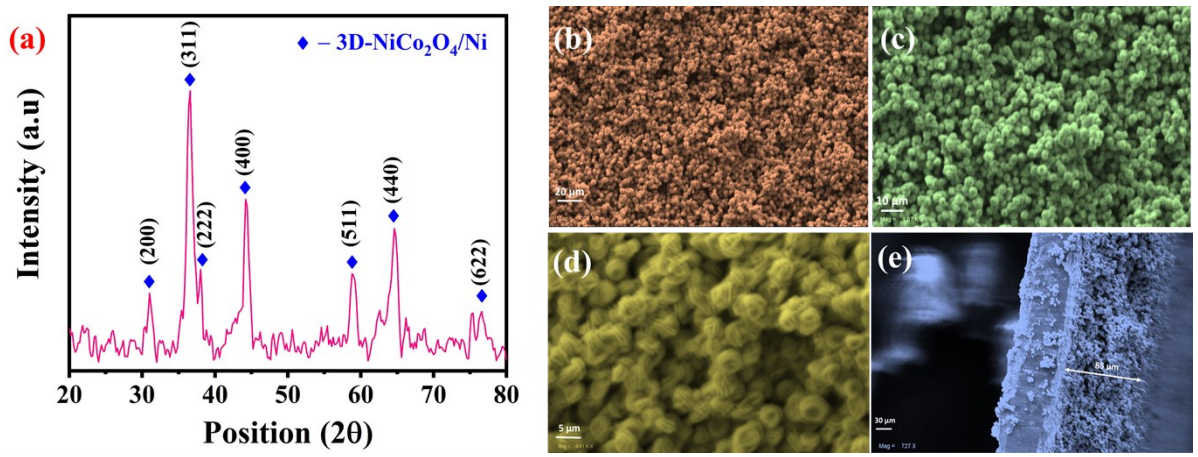

Fig. S8 (a) XRD pattern of 3D-$NiCo_2O_4$/Ni electrode, (b-e) SEM images of 3D-$NiCo_2O_4$ nanostructures at different magnifications (surface and cross-sectional view).

Electrochemical performance of 3D-$NiCo_2O_4$/Ni in three electrode system:

The electrochemical performance of as-prepared 3D-$NiCo_2O_4$/Ni positive electrode were performed in the three-electrode system using a 1 M KOH electrolyte. Fig. S9a shows the cyclic voltammetry performance of 3D-$NiCo_2O_4$/Ni electrode at a scan rate of 5 mV s^{-1} with a pair of redox peaks appeared during the electrochemical process. The observed redox peaks are ascribed to the reversible faradaic redox processes of Ni^{2+}/Ni^{3+} and Co^{2+}/Co^{3+} transitions:

$$NiCo_2O_4 + OH^- + H_2O \leftrightarrow NiOOH + CoOOH + e^- \quad \text{.....(8)}$$

$$CoOOH + OH^- \leftrightarrow CoO_2 + H_2O + e^- \quad \text{..... (9)}$$

The Galvanostatic charge/discharge profiles displays the non-symmetrical shape that indicates the faradaic behaviour of 3D-$NiCo_2O_4$/Ni electrode as shown in Fig. S9b. From the GCD profile, the calculated areal capacitance values of the 3D-$NiCo_2O_4$/Ni electrode are 1.23, 1.05, 0.95, 0.92, 0.91, 0.86, 0.85 and 0.78 F cm^{-2} corresponding areal capacity 678.01, 580.2, 523.8, 511.05, 501.12, 474.05, 471 and 433.6 mC cm^{-2} at current density of 0.5, 1, 2, 3, 4, 5, 7.5, and 10 mA cm^{-2}, respectively. In order to examine the ion/electron transport property of 3D-$NiCo_2O_4$/Ni electrode, electrochemical impedance spectroscopy test was performed in the frequency region of 0.1 Hz to 1 MHz as shown in Fig. S9c. The 3D-$NiCo_2O_4$/Ni electrode revealed the better ion and electron transport process. Furthermore, the 3D-$NiCo_2O_4$/Ni electrode performed with long-term cycling stability at constant current density of 10 mA cm^{-2} for 5000 cycles. The binder-free $NiCo_2O_4$/Ni electrode shows 87.83 % of capacity retention even after 5000 cycles as shown in Fig. S9d, suggesting the better cycling stability.

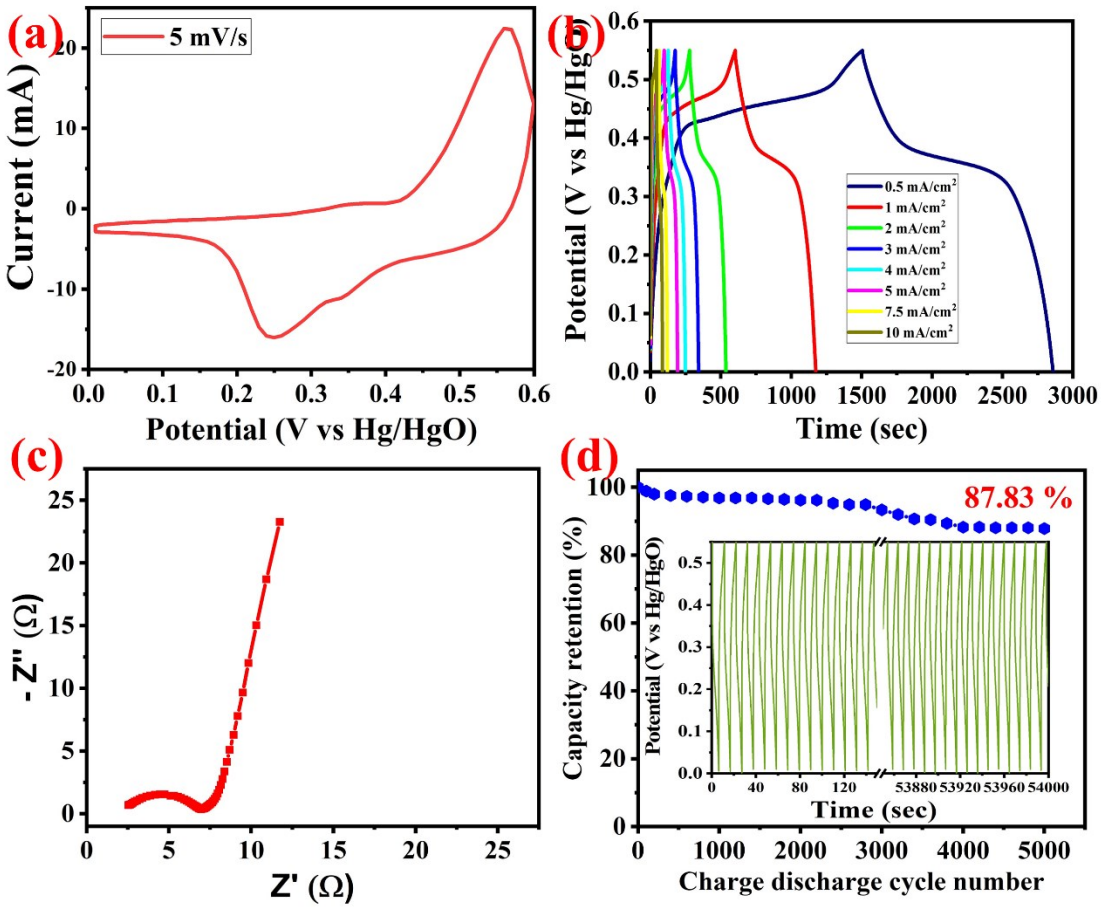

Fig. S9 (a) CV curve of 3D-$NiCo_2O_4$/Ni electrode, (b) GCD curves of 3D-$NiCo_2O_4$/Ni electrode at different current densities (mA cm^{-2}), (c) Nyquist plot of 3D-$NiCo_2O_4$/Ni electrode, and (d) Cycle stability test of the 3D-$NiCo_2O_4$/Ni electrode. Inset is the initial and final cycles.

Hybrid device: 3D-$NiCo_2O_4$||3D-Bi_2O_3

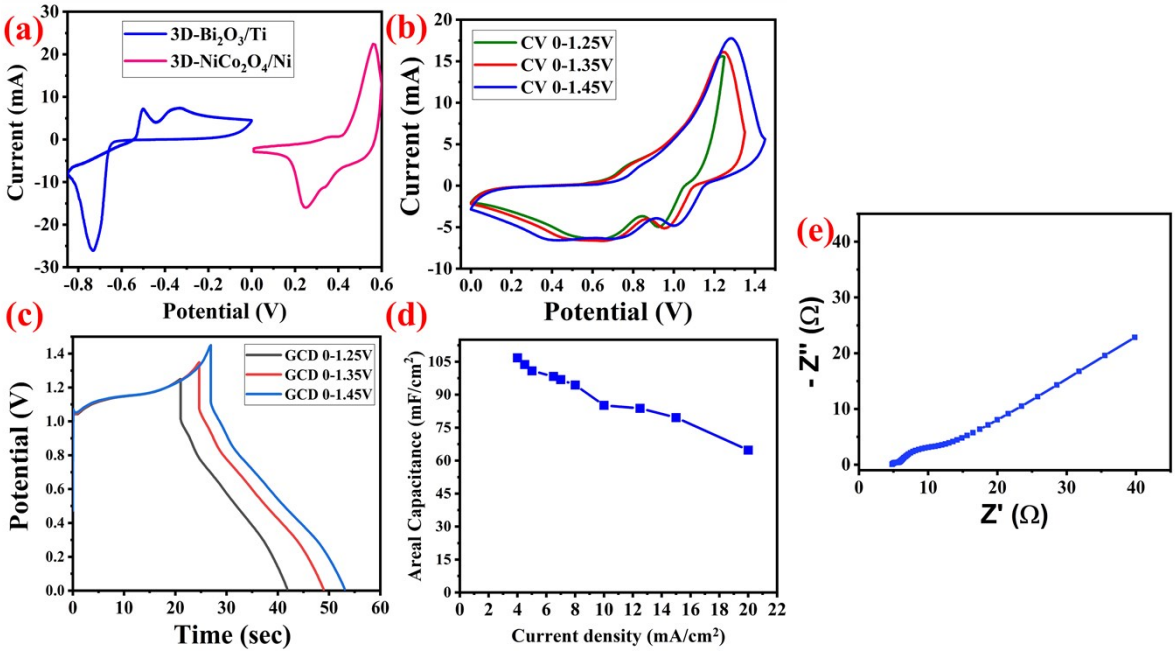

Fig. S10 (a) Comparison CV Curves of 3D-Bi_2O_3/Ti and 3D-$NiCo_2O_4$/Ni electrodes at a scan rate of 10 mV s^{-1}. (b) CV and (c) GCD curves of 3D-$NiCo_2O_4$||3D- Bi_2O_3 hybrid device at various voltages (1.15-1.45 V), (d) Areal capacitance of 3D-$NiCo_2O_4$||3D- Bi_2O_3 hybrid supercapacitors, and (e) Nyquist plot of 3D-$NiCo_2O_4$||3D- Bi_2O_3 hybrid supercapacitors.

Reference:

1. K.-N. Kang, A. Ramadoss, J.-W. Min, J.-C. Yoon, D. Lee, S. J. Kang and J.-H. Jang, *Nano-Micro Letters*, 2020, **12**, 28.
2. W. Raza, S. M. Faisal, M. Owais, D. Bahnemann and M. Muneer, *RSC Advances*, 2016, **6**, 78335-78350.
3. J. Coates, *Encyclopedia of Analytical Chemistry*, 2006, DOI: doi:10.1002/9780470027318.a5606
4. L. Li, X. Zhang, Z. Zhang, M. Zhang, L. Cong, Y. Pan and S. Lin, *Journal of Materials Chemistry A*, 2016, **4**, 16635-16644.
5. X. Wang, J. Hu, W. Liu, G. Wang, J. An and J. Lian, *Journal of Materials Chemistry A*, 2015, **3**, 23333-23344.
6. C. Liu, Z. Xie, W. Wang, Z. Li and Z. Zhang, *Journal of The Electrochemical Society*, 2014, **161**, A1051-A1057.
7. C. Guan, J. Liu, Y. Wang, L. Mao, Z. Fan, Z. Shen, H. Zhang and J. Wang, *ACS Nano*, 2015, **9**, 5198-5207.
8. C. Xia, Q. Jiang, C. Zhao, P. M. Beaujuge and H. N. Alshareef, *Nano Energy*, 2016, **24**, 78-86.
9. P. Yang, Y. Ding, Z. Lin, Z. Chen, Y. Li, P. Qiang, M. Ebrahimi, W. Mai, C. P. Wong and Z. L. Wang, *Nano Letters*, 2014, **14**, 731-736.
10. B. Liu, Y. Wang, H.-W. Jiang and B. Zou, *Journal of Nanomaterials*, 2017, **2017**.
11. F. Wang, X. Zhan, Z. Cheng, Z. Wang, Q. Wang, K. Xu, M. Safdar and J. He, *Small*, 2015, **11**, 749-755.
12. X.-F. Lu, Z.-X. Huang, Y.-X. Tong and G.-R. Li, *Chemical Science*, 2016, **7**, 510-517.
13. J.-X. Feng, S.-H. Ye, X.-F. Lu, Y.-X. Tong and G.-R. Li, *ACS Applied Materials & Interfaces*, 2015, **7**, 11444-11451.

14. M. K. Paliwal and S. K. Meher, *ACS Applied Nano Materials*, 2019, **2**, 5573-5586.
15. H. Xu, X. Hu, H. Yang, Y. Sun, C. Hu and Y. Huang, *Advanced Energy Materials*, 2015, **5**, 1401882.
16. B. Mendoza-Sánchez, T. Brousse, C. Ramirez-Castro, V. Nicolosi and P. S. Grant, *Electrochimica Acta*, 2013, **91**, 253-260.
17. D. Zheng, H. Feng, X. Zhang, X. He, M. Yu, X. Lu and Y. Tong, *Chemical Communications*, 2017, **53**, 3929-3932.
18. M. Qiu, P. Sun, L. Shen, K. Wang, S. Song, X. Yu, S. Tan, C. Zhao and W. Mai, *Journal of Materials Chemistry A*, 2016, **4**, 7266-7273.